Antiferromagnetic quantum spin Hall insulators with high spin Chern numbers

Yang Xue,[1,*] Wei Xu,[2] Bao Zhao,[2,3] Jiayong Zhang,[4] and Zhongqin Yang[2,5]

[1]*Department of Physics, East China University of Science and Technology, Shanghai 200237, China*

[2]*State Key Laboratory of Surface Physics and Key Laboratory of Computational Physical Sciences (MOE) & Department of Physics, Fudan University, Shanghai 200433, China*

[3]*Shandong Key Laboratory of Optical Communication Science and Technology, School of Physics Science and Information Technology, Liaocheng University, Liaocheng 252059, China*

[4]*Jiangsu Key Laboratory of Micro and Nano Heat Fluid Flow Technology and Energy Application, School of Physical Science and Technology, Suzhou University of Science and Technology, Suzhou 215009, China*

[5]*Shanghai Qi Zhi Institute, Shanghai 200030, China*

(Received 10 January 2023; revised 30 May 2023; accepted 3 August 2023; published 17 August 2023)

Topological states in antiferromagnetic (AFM) systems have gained much attention recently. However, general proposals for the realization of a two-dimensional (2D) AFM quantum spin Hall (QSH) insulator are still absent. In this paper, we present a general proposal for 2D AFM QSH insulators by stacking 2D half quantum anomalous Hall insulators in a way that maintains the symmetry of a combination of inversion symmetry and time-reversal symmetry. Depending on the number of stack layers, the obtained AFM QSH insulators can have multiple pairs of dissipationless spin transport channels, revealing the nontrivial implication of high (even) spin Chern numbers (C_s). Using two concrete material examples, Fe_2BrMgP monolayer and TiTe bilayer, we show that both intercalation and van der Waals stacks can be used to realize the proposed AFM QSH insulators. The robustness of the gapless edge states and the topological invariants (high C_s) of our AFM QSH insulators have been tested and shown to be robust against diluted magnetic impurities and weak magnetic field. The spin-chirality-spatial locking phenomenon in the edge states and their susceptibility to z-direction electric field modulation promote these systems as promising candidates for innovative spintronics applications.

DOI: 10.1103/PhysRevB.108.075138

The two-dimensional (2D) topological insulator (TI) or quantum spin Hall (QSH) insulator [1,2], a conceptual landmark of topological states, has inspired the research of exotic topological phenomena and dissipationless spintronics devices for almost two decades [3,4]. The QSH insulator, protected by the time-reversal symmetry $\mathcal{T}$, was characterized by a $\mathbb{Z}_2$ index [1] or a spin Chern number [$C_s = \frac{1}{2}(C_\uparrow - C_\downarrow)$] [5], which have been shown to be equivalent to each other [$\mathbb{Z}_2 = \mathrm{mod}(C_s, 2)$] [6,7]. The two integral values of $\mathbb{Z}_2$ (e.g., 0 and 1) mean that a high C_s greater than 1 will be equivalent to $C_s = 0$ (even C_s) or $C_s = 1$ (odd C_s). This raises the question of whether there is a nontrivial state which has multiple pairs of dissipationless spin transport channels and is characterized by a high C_s [8,9], especially an even high C_s corresponding to a trivial $\mathbb{Z}_2 = 0$ in $\mathcal{T}$-preserved QSH insulators.

3D antiferromagnetic (AFM) TIs have been intensively explored [10–16] and experimentally realized in $MnBi_2Te_4$ [16]. Thus, it is desirable to achieve a 2D AFM QSH insulator in experiments. Recently, the 2D QSH insulator was shown to be robust to the AFM substrates [17] and a 2D AFM topological nonsymmorphic crystalline insulator was proposed to host the gapless edge modes in the nanoribbons, preserving a specific nonsymmorphic symmetry [18]. Can we find a general method to achieve AFM QSH insulators? In a 2D AFM insulator, one cannot define a $\mathbb{Z}_2$ invariant [11] while the C_s can be applied [19]. Is it possible to find a 2D AFM QSH that has a high C_s?

In this paper, we answer these questions affirmatively and provide two types of concrete examples of such an AFM QSH insulator with a high spin Chern number (even). A way to realize a QSH insulator is to create a z-component spin (s_z) conserved superposition of two quantum anomalous Hall (QAH) insulators with equal but opposite magnetic moments [2]. To follow this simple proposal, we consider 2D systems with A-type AFM order, consisting of two identical half-QAH insulators by intercalation or van der Waals (vdW) stacking. Let's assume that our AFM systems have a symmetry of a combination of inversion symmetry $\mathcal{P}$ and $\mathcal{T}$ ($\mathcal{PT}$). The antiunitary $\mathcal{PT}$ symmetry satisfies $(\mathcal{PT})^2 = -1$, leading to the double degeneracy of every band of the 2D system (see Ref. [4] and Appendix A). When the two doubly degenerate bands cross, 2D Dirac points arise, the stability of which is closely related to the crystal symmetries of the systems [4]. If the spin-orbit coupling (SOC) can open the energy gap of Dirac points and maintain the s_z conservation, a QSH insulator with well-defined C_s can be generated.

We first show that the $\mathcal{PT}$ symmetry can decouple different spin spaces with $s_z = \pm 1/2$ while maintaining the conservation of s_z in a $\mathcal{PT}$ pair. Without loss of generality, we set the local magnetic moments of the top and bottom ferromagnetic (FM) layers along $+z$ and $-z$ directions, respectively. When the SOC effect is ignored, s_z is well-defined and each eigenstate $\psi(k)$ and its $\mathcal{PT}$ partner, $\mathcal{PT}\psi(k)$, have opposite s_z

*xuey@ecust.edu.cn

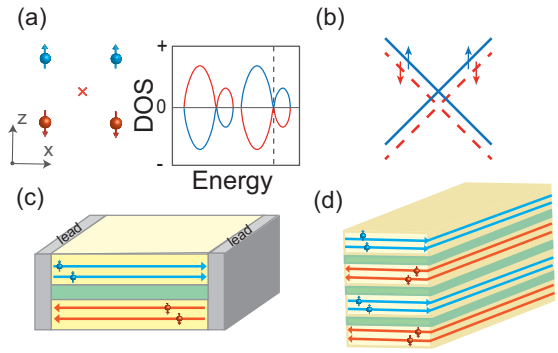

FIG. 1. The illustration for the effect of the $\mathcal{PT}$ symmetry in real space and reciprocal space (a) and for the energy bands near a Dirac point (b) for the $\mathcal{PT}$-symmetric stacked half QAH insulators. In the DOS, the dashed line denotes the Fermi level, and positive (negative) DOS are for the upper (lower) QAH insulator. The line type (dashed or solid) in (b) denotes the irreducible representations for the bands. (c) The illustration for the spin-chirality-spatial locked edge states of the AFM QSH insulators with a high C_s, where the yellow and green regions represent the identical stacked QAH insulators and the intercalation (vdW gap), respectively. (d) same as (c), but for a multilayer stacking AFM QSH insulator. Blue and red represent spin up and spin down, respectively.

values. When SOC is included, the eigenstates of the system at every k point are also paired according to $\mathcal{PT}$. Under the basis of a $\mathcal{PT}$ doublet $\{\psi(k), (\mathcal{PT})\psi(k)\}$, the $\mathcal{PT}$ operator takes the form of $-i\sigma_y = \left(\begin{smallmatrix} 0 & -1 \\ 1 & 0 \end{smallmatrix}\right)$ (for details, see Appendix A). The anticommutative relation between $\hat{s}_z$ and $\mathcal{PT}$, $\{\mathcal{PT}, \hat{s}_z\} = 0$, lead to the form of $\hat{s}_z$, under this basis to be chosen as $\frac{\hbar}{2}\sigma_z = \frac{\hbar}{2}\left(\begin{smallmatrix} 1 & 0 \\ 0 & -1 \end{smallmatrix}\right)$. As a result, we can easily obtain the relation between the two eigenstates of $\hat{s}_z$ $\{\chi_\uparrow(k), \chi_\downarrow(k)\}$ and the $\mathcal{PT}$ doublet $\{\psi(k), (\mathcal{PT})\psi(k)\}$ as follows:

$$\begin{aligned} \chi_\uparrow(k) &= \psi(k), \\ \chi_\downarrow(k) &= (\mathcal{PT})\psi(k), \end{aligned} \tag{1}$$

The interaction between the pair $\{\chi_\uparrow(k), \chi_\downarrow(k)\}$ is then given as

$$\begin{aligned} &\langle\chi_\uparrow(k)|\hat{H}|\chi_\downarrow(k)\rangle \\ &= \langle\psi(k)|\hat{H}|(\mathcal{PT})\psi(k)\rangle \\ &= \langle\psi(k)|(\mathcal{PT})|\hat{H}\psi(k)\rangle \\ &= E(k)\langle\psi(k)|(\mathcal{PT})\psi(k)\rangle = 0, \end{aligned} \tag{2}$$

which means that the s_z up state and s_z down state are decoupled from each other in a $\mathcal{PT}$ pair.

Let's consider a Dirac point in a $\mathcal{PT}$ symmetric system created by stacking two half (fully spin-polarized) QAH insulators [20–23]. As shown in Fig. 1(a), the half property of the single QAH insulator results in the approximate isolation of its spin-up and spin-down bands. The $\mathcal{PT}$ symmetry ensures that the spin-up bands from top layer $\psi^T_{i,\uparrow}(\mathbf{k}) = \sum_{\mathbf{R}} e^{i\mathbf{k}\cdot\mathbf{R}} w_{i,\uparrow}(\mathbf{r} - \mathbf{R})$ are degenerate with the spin-down bands from bottom layer $\psi^B_{\mathcal{P}i,\downarrow}(\mathbf{k}) = \mathcal{PT}\psi^T_{i,\uparrow}(\mathbf{k}) = \sum_{\mathbf{R}} e^{i\mathbf{k}\cdot\mathbf{R}} w_{\mathcal{P}i,\downarrow}(\mathbf{r} - \mathbf{R})$ near the Fermi level (E_F), where i and $\mathcal{P}i$ denote the sites of orbital w_i in the top layer and the sites of orbital $w_{\mathcal{P}i}$ in the bottom layer, respectively. As shown in Fig. 1(b), the energy bands with the same s_z in the two branches of the Dirac point come from the same QAH insulator and have the same irreducible representations. As we discussed above, the $\mathcal{PT}$ symmetry leads to states with different s_z in one branch being orthogonal to each other and belonging to different irreducible representations. Eventually, the $\mathcal{PT}$ symmetry and the half property of the constituent units enable the binding of the spin and representation of the energy bands near this Dirac point. This means that energy bands with different spins have different representations, while energy bands with the same spin have the same representation. Thus, the SOC maintains the conservation of s_z and can only open energy gaps within the states with the same s_z in this stacked system. Since all the occupied states in a single spin channel have nontrivial winding numbers, a unique AFM QSH insulator emerges. Note that states with different s_z are decoupled, so winding numbers greater than 1 in a single spin channel become meaningful, and similarly for C_s greater than 1. The high C_s will result in multiple pairs of dissipationless spin transport channels. More interestingly, a spin-chirality-spatial locking phenomenon appears in the edge states of this AFM QSH insulator. The edge states in the half-QAH insulator are fully spin polarized, whose spin directions are locked with their chirality [20]. These above elements together lead to the spin-chirality-spatial locking phenomenon in edge states, where transport channels with different spins have different chirality and spatial distribution regions, as shown in Fig. 1(c). The number of such spin transport channels, as well as the C_s, can be further extended by increasing the number of stacked layers, as shown in Fig. 1(d).

Our first-principles density functional theory (DFT) calculations are carried out with the generalized gradient approximation proposed by Perdew, Burke, and Ernzerhof (PBE) [24], which is implemented in the VIENNA AB INITIO SIMULATION PACKAGE [25]. The GGA + U method [26] is employed to describe the correlated Fe and Ti 3d electrons, and the value of the on-site Coulomb interaction U and exchange interaction J are set to 2.5 (3.0) and 0.0 (0.0) eV for Fe [23] (Ti [22]), respectively. The plane-wave cutoff energy was set to 500 eV and the vacuum space is more than 15 Å to avoid the influence between two adjacent slabs. The force converge criterion was less than 0.01 eV/Å, the energies were less than 10^{-6} eV, and Monkhorst-Pack k-point grids of $12\times12\times1$ were adopted for the calculations. The vdW interaction functional using the method of DFT-D3 is employed in the vdW heterostructure calculations. The tight-binding (TB) model and edge states are calculated by WANNIER90 [27] and WANNIERTOOLS [28], respectively. The hybrid functional HSE06 [29] is used to verify band structure. The phonon spectra is calculated by using density functional perturbation theory (DFPT) implemented in the PHONOPY package [30,31], with $3\times3\times1$ supercell.

In accordance with our analysis, we discover that the AFM insulators Fe_2XYP monolayer (X = Br, Cl or I, Y = Mg, Be) and TiTe bilayer can host the QSH effect with high C_s, which could simply be viewed as the intergrowth of MgP between double layers of half Chern insulator FeX [23] and the vdW stacking of double layers of half Chern insulator TiTe [22], respectively. In contrast to the previously theoretically reported topological semimetals with WC-type hexagonal structure

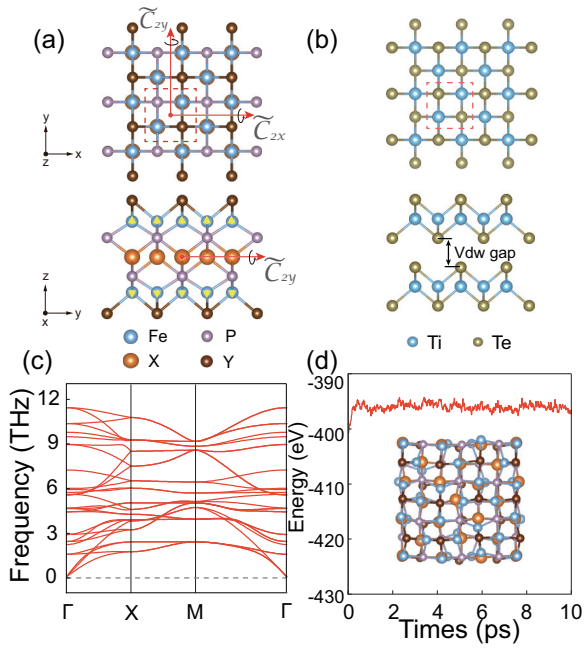

FIG. 2. Top and side views of the Fe_2XYP monolayer (X = Br, Cl or I, Y = Mg, Be) (a) and of the TiTe bilayer vdW heterostructure (b) with A-type AFM ordering of magnetic atoms, respectively. The yellow arrows in (a) denote the atomic spin moments aligned or antialigned with the z axis. The red dot in (a) represents the $\mathcal{PT}$ center. (c) Phonon spectra for the Fe_2BrMgP monolayer, showing that the Fe_2BrMgP monolayer is dynamically stable. (d) The energy evolution curves for the Fe_2BrMgP monolayer. The insets display snapshots of the final frames for the Fe_2BrMgP monolayer.

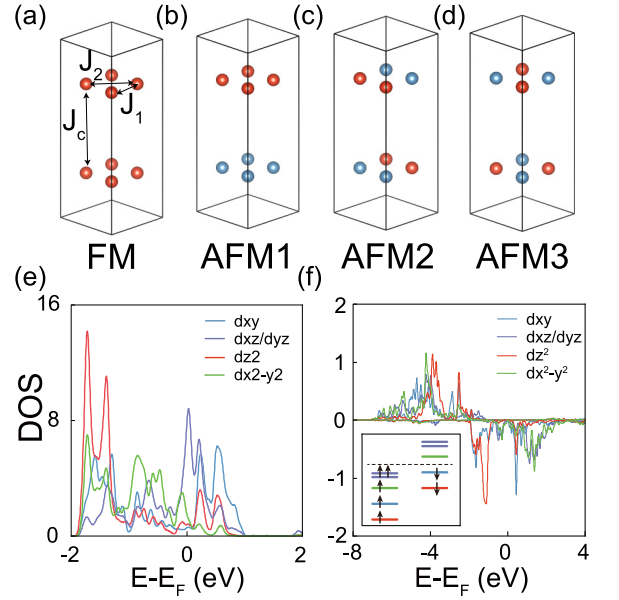

FIG. 3. (a)–(d) Possible magnetic configurations considered: ferromagnet (FM), A-type antiferromagnet (AFM1), C-type antiferromagnet (AFM2), and G-type antiferromagnet (AFM3). Red and blue dots denote the magnetic atoms with opposite magnetization directions. The exchange interactions J_1, J_2, and J_c are indicated by black arrows. (e) and (f) are orbital resolved DOS for Fe atoms of the Fe_2BrMgP monolayer with a nonmagnetic and AFM1 ground state, respectively, where the d_{xz} and d_{yz} orbitals are degenerate. Inset in (f) shows the d-orbital distribution of Fe atoms with the E_F labeled with a dashed line.

(space group $P\bar{6}m2$ and No. 187) [32], the recently theoretically proposed FeX and TiTe monolayers are half-QAH insulators with space group $P4/nmm$ (No. 129) [22,23]. The crystal structures of these two types of AFM insulators are shown in Figs. 2(a) and 2(b). The optimized lattice constants of the different Fe_2XYP monolayers are listed in Table I. The phonon spectra [Fig. 2(c)] without imaginary frequency mode manifests the dynamical stability of the Fe_2XYP monolayer. The thermal stability of Fe_2XYP monolayer is further confirmed by first-principles molecular-dynamics simulation [Fig. 2(d)], which shows that the structure remains intact at a temperature of 300 K after 10 ps. To determine their magnetic ground states, the $\sqrt{2}\times\sqrt{2}\times1$ supercell of these twos type of AFM insulators with four magnetic configurations are considered, as shown in Figs. 3(a)–3(d). The magnetic moment of Fe_2BrMgP monolayer is $3\mu_B$ per Fe atom from our DFT calculations. This can be understood by analyzing the valence electron configuration of the Fe atom ($3d^7 4s^0$) after transferring $1e^-$ to nonmagnetic atoms. The crystal field of the Fe atom $2mm$ causes the five d orbitals of the Fe atom to split into four low to high energy groups $d_{z^2} < d_{xy} < d_{x^2-y^2} < d_{xz/yz}$ [Fig. 3(e)]. As shown in the inset of Fig. 3(f), five unpaired $3d$ electrons are to first occupy four energy levels to have high spin alignment based on Hund'âs rules. Then, the two left $3d$ electrons will occupy the lowest d_{z^2} and d_{xy} levels, leading to three unpaired $3d$ electrons ($3\mu_B$), which can be seen in the partial density of states (DOS) of the Fe_2BrMgP monolayer [Fig. 3(f)]. It is found that their ground magnetic states are all A-type AFMs, which is well understood by the Goodenough-Kanamori-Anderson rules [33–35]. The in-plane bond angle between two nearest Fe (Ti) atoms is close to 90° and is expected to induce FM ordering. On the contrary, Fe (Ti) atoms between neighboring atomic layers are coupled through an effective bond with a 180° bonding angle, where AFM ordering is induced. The Neel temperature for the Fe_2BrMgP monolayer is ∼125 K, shown in Fig. 4(b), whose calculation details can be seen in Appendix C. The unit cells all have No. 129.419 magnetic space group, which has the typical $\mathcal{PT}$ symmetry and two screw symmetries $\widetilde{C}_{2x} = \{C_{2x}|a/2\}$ and $\widetilde{C}_{2y} = \{C_{2y}|b/2\}$.

By calculating the electronic band structures of the Fe_2BrMgP monolayer without SOC, one observes two pairs of

TABLE I. The optimized lattice constants and energy gap calculated by PBE+U with SOC for the Fe_2XYP monolayer with different X and Y atoms.

X	Y	Lattice constant (Å)	Energy gap (meV)
Be	Cl	3.67	140.9
Be	Br	3.70	165.5
Be	I	3.76	200.9
Mg	Cl	4.01	231.4
Mg	Br	4.03	258.4
Mg	I	4.06	281.4

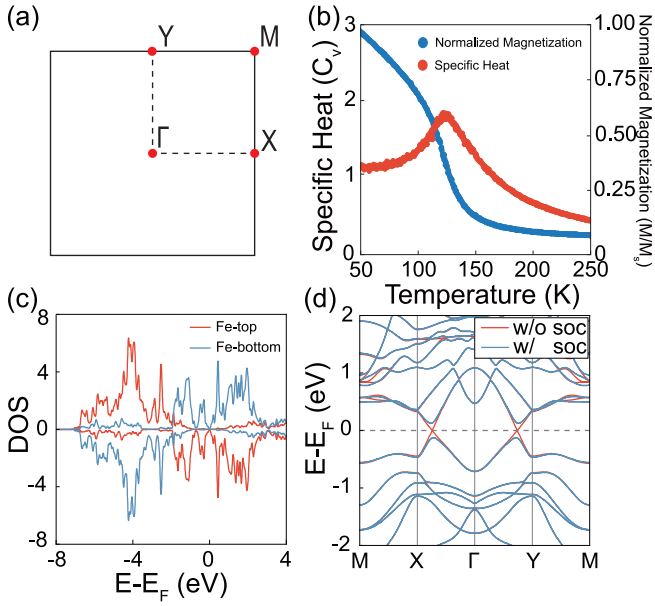

FIG. 4. (a) The first BZ with high-symmetry points and lines for the Fe_2XYP monolayer. (b) The normalized average magnetic moment (blue curve) and specific heat (red curve) versus temperature for the Fe_2BrMgP monolayer. (c) Spatially resolved DOS for the Fe_2BrMgP monolayer without SOC, where Fe top (bottom) stands for Fe atoms of the top (bottom) layer. (d) The energy bands of the Fe_2BrMgP monolayer without and with SOC.

fourfold band-crossing points near E_F. These crossing points, representing 2D Dirac points, are symmetrically distributed on the x axis and the y axis in Fig. 4(d) and are related to each other by $\widetilde{C}_{4z} = \{C_{4z}|(a/2,\ 0,\ 0)\}$. As shown in the DOS in Fig. 4(c), the low-energy bands originating from the same FM plane exhibit half properties. The bands on the upper and lower FM planes have different s_z and are degenerate with each other. The $\widetilde{C}_{2x}$ leads to the $\mathcal{PT}$ pairs at the k-path invariant under $\widetilde{C}_{2x}$ to have different eigenvalues of $\widetilde{C}_{2x}$. As a result, the Dirac points at the $\widetilde{C}_{2x}$ invariant k points are not stable and can be gapped by SOC, the same results for those at the $\widetilde{C}_{2y}$ invariant k points, shown in Fig. 4(d) (for details, see Appendix B). The gap opening at a 2D Dirac point in Fig. 4(d) is about 258 meV. In general, a Dirac point located at the n-fold rotation invariant momentum is usually not stable and can be gapped by SOC for $n = 2, 4, 6$. To characterize the low-energy band structures near a 2D Dirac point, we construct a $k \cdot p$ effective model. The effective Hamiltonian for a 2D Dirac point in $\Gamma - X$ is subjected to the magnetic little cogroup $2/m'$ of $\Gamma - X$, with two generators, $\widetilde{C}_{2x}$ and $\mathcal{PT}$. The symmetry constraints are given by

$$\begin{aligned} \widetilde{C}_{2x}^{-1} H(q_x, q_y) \widetilde{C}_{2x} &= H(q_x, -q_y), \\ \mathcal{PT}^{-1} H(q_x, q_y) \mathcal{PT} &= H^*(-q_x, -q_y), \end{aligned} \tag{3}$$

where $\mathbf{q}$ is measured from the 2D Dirac point in $\Gamma - X$. In the basis of the calculated irreducible representations near the Dirac point $\{\overline{\mathrm{DT}}3\overline{\mathrm{DT}}4, \overline{\mathrm{DT}}3\overline{\mathrm{DT}}4\}$, we find that the effective model for the non-SOC part up to second order in $\mathbf{q}$ and the SOC part up to first order in $\mathbf{q}$ is given by

$$H(q_x, q_y) = H_0 + H_{\mathrm{SOC}}, \tag{4}$$

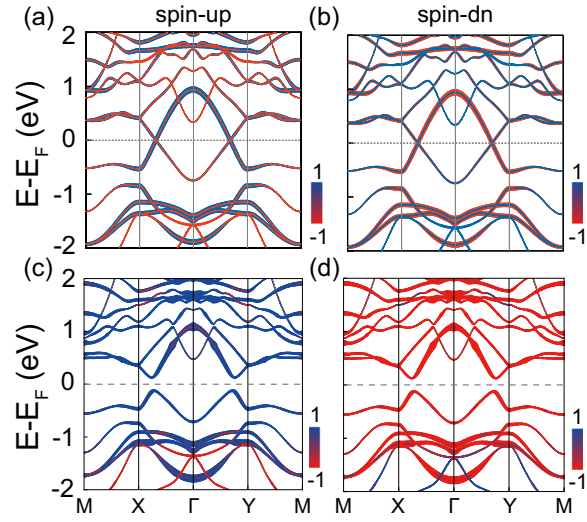

FIG. 5. Spin-spatial resolved projected band structures for the Fe_2BrMgP monolayer without SOC [(a), (b)] and with SOC [(c), (d)]. (a) and (c) are for the spin-up projection, (b) and (d) for the spin-down projection. Red and blue stand for projections of the Fe atoms in the top and bottom layers, respectively.

where $H_0 = h_1\sigma_0 \otimes \sigma_z + h_2\sigma_0 \otimes \sigma_y$, $h_1 = (Aq_x + Bq_x^2 + Cq_y^2)$, and $h_2 = (Dq_y + Eq_xq_y)$. The $H_{\mathrm{SOC}} = H_{\mathrm{SOC1}} + H_{\mathrm{SOC2}} = \Lambda_1\sigma_z \otimes \sigma_x + \Lambda_2\sigma_y \otimes \sigma_x$, where $\Lambda_1 = -(\lambda_{10} + \lambda_{11}q_x)$ and $\Lambda_2 = (\lambda_{20} + \lambda_{21}q_x)$. The h_1 term represents the linear and quadratic terms of the dispersion near the Dirac point. The h_2 term is the coupling term. The SOC term H_{SOC} can be divided into a spin-conserved SOC term H_{SOC1} and a spin-mixing SOC term H_{SOC2}. The H_{SOC2} is negligibly small (see Fig. 5) due to the $\mathcal{PT}$ symmetry and the half property of the constituent units (QAH insulators). After dropping the negligibly small spin-mixing SOC term H_{SOC2}, the eigenenergies of the Hamiltonian are given as $E_\pm = \pm\sqrt{h_1^2 + h_2^2 + \Lambda_1^2}$, whose corresponding eigenstates can be classified into two types: $\Psi_\pm^T = [-\frac{i(h_1 \pm \sqrt{h_1^2+h_2^2+\Lambda_1^2})}{h_2+i\Lambda_1}, 1, 0, 0]^\intercal$ and $\Psi_\pm^B = [0, 0, -\frac{i(h_1 \pm \sqrt{h_1^2+h_2^2+\Lambda_1^2})}{h_2-i\Lambda_1}, 1]^\intercal$. At the Dirac point, where $q_x = q_y = 0$, a gap is given as $\Delta E = 2|\lambda_{10}|$. Due to the similar low-energy electronic structures of the two proposed types of AFM insulators, we will focus on the Fe_2BrMgP monolayer in the following sections. Corresponding results for other materials can be found in Fig. 8.

To confirm the the topologically nontrivial character of the gap, the spin Hall conductivity σ_{xy}^S is calculated using the Kubo formula [36,37]:

$$\begin{aligned} \sigma_{xy}^S &= \frac{e\hbar}{(2\pi)^2} \int \Omega_{xy}^S(\mathbf{k}) d^2k, \\ \Omega_{xy}^S(\mathbf{k}) &= \sum_n f_{nk} \Omega_{n,xy}^S(\mathbf{k}), \\ \Omega_{n,xy}^S(\mathbf{k}) &= \hbar^2 \sum_{m \neq n} \frac{-2Im\left[\langle nk|\frac{1}{2}\{\hat{\sigma}_z, \hat{v}_x\}|mk\rangle\langle mk|\hat{v}_y|nk\rangle\right]}{(\epsilon_{nk} - \epsilon_{mk})^2}. \end{aligned} \tag{5}$$

Here, v_i is the ith Cartesian component of the velocity operator, f_{nk} is the Fermi-Dirac distribution function, and

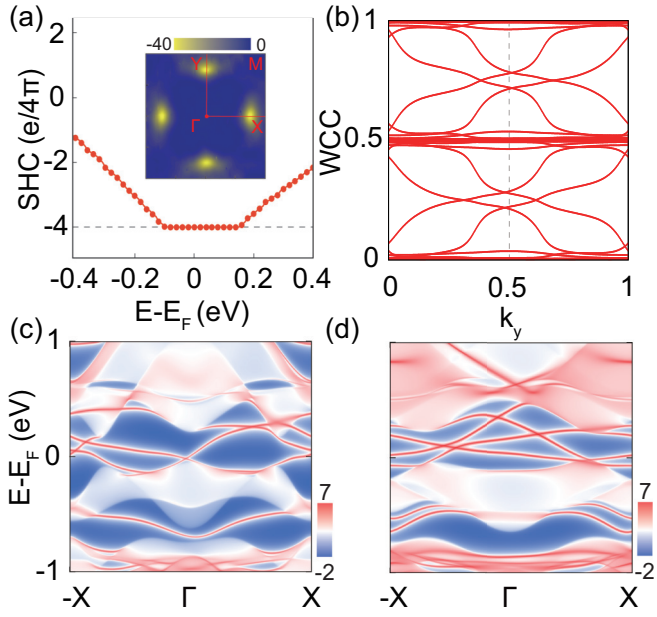

FIG. 6. (a) Energy dependence of the spin Hall conductivity σ_{xy}^{S}, showing a quantized value within the energy window of the SOC gap. (Inset) K-space distribution of spin Berry curvature within the SOC gap. (b) Evolution of WCCs for the Fe_2BrMgP monolayer along k_y. (c) and (d) The edge states of a semi-infinite Fe_2BrMgP monolayer cut along the [100] and [120] direction, respectively.

$J_x^S = (\hbar/4)\{\hat{\sigma}_z, \hat{v}_x\}$ describes a spin current flowing in the x direction, with the spin polarization perpendicular to the plane. The curly brackets in the expression for J_x^S stand for an anticommutator. Figure 6(a) displays the σ_{xy}^S as a function of the Fermi level in a Fe_2BrMgP monolayer. The quantization of σ_{xy}^S within the insulating region arises mainly from the spin Berry curvature $\Omega_{xy}^S(\mathbf{k})$ near the Dirac points at the k lines $(-X) \to X$ and $(-Y) \to Y$, as shown in the inset of Fig. 6(a). This quantization demonstrates the nontrivial band topology of Fe_2BrMgP monolayer. The calculated σ_{xy}^S within the insulating region is strictly equal to -4 in unit of $e/(4\pi)$, indicating that there is no coupling between states with different s_z, which is consistent with the analysis presented earlier. The $\sigma_{xy}^S = -4$ also demonstrates that the Fe_2BrMgP monolayer has a high spin Chern number $C_s = (2\pi/e)\sigma_{xy}^S = -2$, which is confirmed by the Wannier charge center (WCC) of the Fe_2BrMgP monolayer in Fig. 6(b). Due to the lack of $\mathcal{T}$ symmetry, there is no Kramers degeneracy of the WCC at the $\mathcal{T}$-invariant momentum. However, no gap opening occurs at the crossing points of the WCC spectra, indicating that the Chern numbers defined for each s_z space are robust and nontrivial ($C_\uparrow = -2$ and $C_\downarrow = 2$). The robustness of the crossing points of the WCC spectra is also tested by adding an s_z mixing term $M\sigma_x$ into the pristine Hamiltonian of the Fe_2BrMgP monolayer, which represents a uniform FM exchange field along the x direction (M is the strength of the exchange field). The obtained results, shown in Fig. 7(c), demonstrate that M not more than 0.05 eV will not open the gap of the crossing points of the WCC.

$C_s = -2$ suggests that two pairs of gapless edge states with opposite chiralities appear in the bulk gap [Figs. 6(c) and 6(d)]. The edge states with different chiralities come from the spin spaces with different s_z, which are decoupled from each other by $\mathcal{PT}$ symmetry and the half property of the constituent units (QAH insulators). The two independent spin spaces with different s_z can be viewed as two fully decoupled QAH insulators with opposite chiralities. The appearance of the gapless edge states of the QAH insulator is unaffected by its boundary shape. Hence, the appearance of the gapless edge states in our $\mathcal{PT}$-symmetric AFM-QSH insulators also has no special requirements on the shape of the boundary, see Figs. 8(e) and 8(f). To break the $\mathcal{PT}$ symmetry, a small uniform external vertical electric field of 0.005 eV/Å is applied to the system, which can induce relatively significant gaps for edge states, as shown in Fig. 7(f).

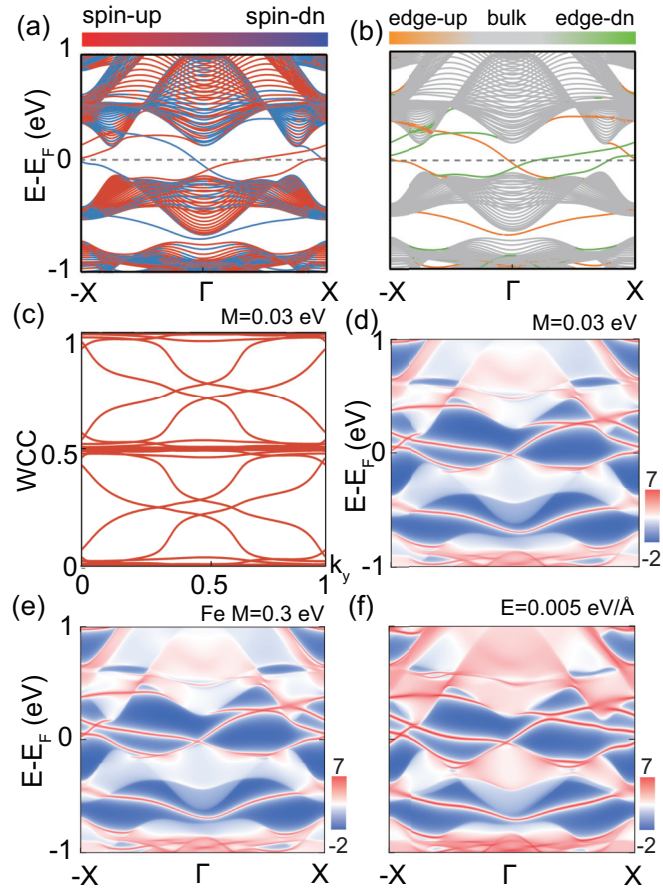

FIG. 7. (a) Spin-resolved and (b) localization-resolved band structures of one-dimensional nanoribbon for Fe_2BrMgP monolayer with SOC. The projections are only applied for one side of the nanoribbon. Color in (a) from blue to red indicating the spin polarization on the edge with the expectation value of σ_z, and in (b) from gray to yellow or green represents the weight of atoms located from the middle to top or bottom regions at one edge of the ribbon structures. (c) Evolution of WCCs for the Fe_2BrMgP monolayer along k_y with applied strength of 0.03 eV x-direction FM exchange field. (d), (e), and (f) are the edge states of a semi-infinite Fe_2BrMgP monolayer cut along the [100] with applied strength of 0.03 eV FM exchange field in x-direction, strength of 0.3 eV magnetic impurities at an Fe atom site at the boundary, and strength of 0.005 eV/Å z-direction electric field, respectively. Mid-gap edge states in (d) and (e) remain gapless while in (f) are gapped.

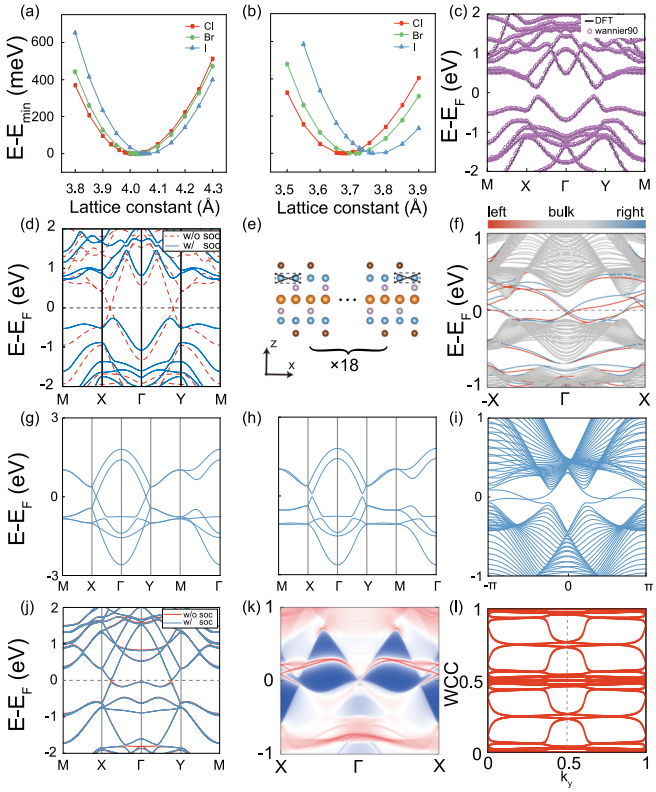

FIG. 8. (a), (b) Total energies as a function of the lattice constant for the Fe_2XMgP and the Fe_2XBeP monolayers with $X =$ Cl, Br, and I, respectively, in which the minimum total energy at the equilibrium lattice constant for each case is set as energy zero. Band structures of the Fe_2BrMgP monolayer using WANNIER90 (c) and HSE06 (d). (e) Sketch of the one-dimensional nanoribbons of the Fe_2BrMgP monolayer for the edge states, where the dashed boxes mark the columns of atoms removed at the nanoribbon boundaries. (f) Localization-resolved band structures for (e), where the color from gray to red or blue indicates the weight of atoms located from the middle to the left or right regions of the ribbon structures. (g) The fitted bands for the case without SOC, based on our TB model with the following parameters: $V_{dd\pi} = 0.05\,\text{eV}$, $V_{dd\sigma} = 0.2\,\text{eV}$, $V_{dd\delta} = -0.2\,\text{eV}$, $\epsilon_p = -2.5\,\text{eV}$, $\epsilon_{xy} = -0.434\,\text{eV}$, $\epsilon_{z^2} = 0.366\,\text{eV}$, $\epsilon_{x^2-y^2} = -1\,\text{eV}$, $\lambda_p = 0\,\text{eV}$, $\lambda_d = 0\,\text{eV}$, $V_{pd\pi} = -0.7l\,\text{eV}$, $V_{pd\sigma} = 4.8(l^3 - 1.732)/(1 - 8\tau^2)\,\text{eV}$. (h) The fitted bands for the case with SOC, using the same parameters as (g) except for $\lambda_p = 0.375\,\text{eV}$, $\lambda_d = 0.05\,\text{eV}$. (i) The calculated one-dimensional nanoribbon for (h). (j)–(l) are results for the A-type AFM TiTe bilayer: band structures (j), the edge states of a semi-infinite TiTe bilayer cut along the [100] direction (k), and evolution of WCCs along k_y (l).

To further understand the nontrivial topological properties of our systems, a TB model was built. For our system, the low-energy bands near E_F can be regarded as deriving from two decoupled and equal layers with opposite magnetic moments. Thus, we can derive our low-energy effective TB model with the basis in a single layer and a single spin channel. Due to the low-energy dispersions mainly consisting of the d_{z^2}, $d_{x^2-y^2}$, and d_{xy} orbitals of the magnetic atoms, which form three bases of the point group, we adopted the basis as $\{M1 - d_{x^2-y^2}\uparrow, M1 - d_{xy}\uparrow, M1 - d_{z^2}\uparrow, M2 - d_{x^2-y^2}\uparrow, M2 - d_{xy}\uparrow, M2 - d_{z^2}\uparrow, X1 - p_x\uparrow, X1 - p_y\uparrow, X2 - p_x\uparrow, X2 - p_y\uparrow\}$ for our TB model. $M1$ and $M2$ represent two magnetic atoms in the same layer with coordinates $(1/4, 1/4, z)$ and $(3/4, 3/4, z)$, respectively, and $X1$ and $X2$ represent two other nonmagnetic atoms in the same layer with coordinates $(1/4, 3/4, z + \tau)$ and $(3/4, 1/4, z - \tau)$, respectively, as shown in Fig. 2(a). Under this basis, the total Hamiltonian can be written as

$$H(k) = \begin{bmatrix} H_d & T_{pd} \\ T_{pd}^{\dagger} & H_p \end{bmatrix}, \tag{6}$$

where H_d represents the nearest-neighbor (NN) hopping terms and on-site SOC terms of the d orbitals of the magnetic atoms in one layer, H_p corresponds to the on-site energy and on-site SOC terms of the p orbitals of the nonmagnetic atoms in the same layer. T_{pd} denotes the NN hopping terms between the d and p orbitals in this layer. It is worth noting that we neglected the NN hopping between the $p_{x/y}$ orbitals in H_p due to the significant difference in on-site energy between the p and d orbitals, which prevents the d electrons from hopping through the p orbitals.

Then H_d can be expressed as follows:

$$H_d = \begin{bmatrix} \epsilon_{x2-y2} & -2i\lambda_d & 0 & h_{14} & 0 & 0 \\ 2i\lambda_d & \epsilon_{xy} & 0 & 0 & h_{25} & h_{26} \\ 0 & 0 & \epsilon_{z^2} & 0 & h_{26} & h_{36} \\ h_{14} & 0 & 0 & \epsilon_{x2-y2} & -2i\lambda_d & 0 \\ 0 & h_{25} & h_{26} & 2i\lambda_d & \epsilon_{xy} & 0 \\ 0 & h_{26} & h_{36} & 0 & 0 & \epsilon_{z^2} \end{bmatrix}, \tag{7}$$

where $h_{14} = 4V_{dd\pi}\cos(\frac{k_x}{2})\cos(\frac{k_y}{2})$, $h_{25} = (3V_{dd\sigma} + V_{dd\delta})\cos(\frac{k_x}{2})\cos(\frac{k_y}{2})$, $h_{26} = -\sqrt{3}(V_{dd\delta} - V_{dd\sigma})\sin(\frac{k_x}{2})\sin(\frac{k_y}{2})$, and $h_{36} = (3V_{dd\delta} + V_{dd\sigma})\cos(\frac{k_x}{2})\cos(\frac{k_y}{2})$.

T_{pd} can be written as

$$T_{pd} = \begin{bmatrix} 0 & t_{12} & t_{13} & 0 \\ t_{21} & 0 & 0 & t_{24} \\ 0 & t_{32} & t_{33} & 0 \\ t_{13} & 0 & 0 & t_{12} \\ 0 & t_{24} & t_{21} & 0 \\ t_{33} & 0 & 0 & t_{32} \end{bmatrix}, \tag{8}$$

where $t_{12} = i[\frac{\sqrt{3}}{8l^3}V_{pd\sigma} + (l - \frac{1}{4l^3})V_{pd\pi}]\sin(\frac{k_y}{2})$, $t_{13} = -i[\frac{\sqrt{3}}{8l^3}V_{pd\sigma} + (l - \frac{1}{4l^3})V_{pd\pi}]\sin(\frac{k_x}{2})$, $t_{21} = -i\frac{1}{l}V_{pd\pi}\sin(\frac{k_y}{2})$, $t_{24} = -i\frac{1}{l}V_{pd\pi}\sin(\frac{k_x}{2})$, $t_{32} = i\frac{1}{l^3}[\sqrt{3}V_{pd\pi} + (\frac{1}{8} - \tau^2)V_{pd\sigma}]\sin(\frac{k_y}{2})$, and $t_{33} = i\frac{1}{l^3}[\sqrt{3}V_{pd\pi} + (\frac{1}{8} - \tau^2)V_{pd\sigma}]\sin(\frac{k_x}{2})$.

The H_p can be written as

$$H_p = \begin{bmatrix} \epsilon_p & -i\lambda_p & 0 & 0 \\ -i\lambda_p & \epsilon_p & 0 & 0 \\ 0 & 0 & \epsilon_p & -i\lambda_p \\ 0 & 0 & -i\lambda_p & \epsilon_p \end{bmatrix}. \tag{9}$$

In the above statement, $\epsilon_{x2-y2/xy/z^2}$ and ϵ_p represent the on-site energy of $d_{x^2-y^2/xy/z^2}$ and $p_{x/y}$ orbitals, respectively. The parameters λ_d and λ_p denote the strength of the

atomic SOC of these orbitals, respectively. The parameters $V_{dd\pi/\sigma/\delta}$ and $V_{pd\pi/\sigma/\delta}$ correspond to the standard Slater-Koster hopping parameters for the NN $\pi/\sigma/\delta$ bonds between the $d-d$ orbitals and $p-d$ orbitals, respectively. l represents the distance between the magnetic atoms and their NN nonmagnetic atoms.

Through the downfolding procedure, we can obtain the low-energy effective Hamiltonian as follows:

$$H_{\text{eff}} \approx H_d - T_{pd} H_p^{-1} T_{pd}^{\dagger} \tag{10}$$

$$= \frac{1}{\epsilon_p^2 - \lambda_p^2} \begin{bmatrix} H_{11} & H_{12} & H_{13} & H_{14} & 0 & H_{16} \\ -H_{12} & H_{22} & H_{23} & 0 & H_{25} & H_{26} \\ H_{13} & -H_{23} & H_{33} & -H_{16} & H_{26} & H_{36} \\ H_{14} & 0 & H_{16} & H_{11} & H_{12} & H_{13} \\ 0 & H_{25} & H_{26} & -H_{12} & H_{22} & H_{23} \\ -H_{16} & H_{26} & H_{36} & H_{13} & -H_{23} & H_{33} \end{bmatrix}, \tag{11}$$

where $H_{11} = \epsilon_{x2-y2} - \epsilon_p(|t_{12}|^2 + |t_{13}|^2)$, $H_{12} = -2i\lambda_d + i\lambda_p(t_{12}t_{21}^* - t_{13}t_{24}^*)$, $H_{13} = -\epsilon_p(t_{12}t_{32}^* + t_{13}t_{33}^*)$, $H_{14} = h_{14}$, $H_{16} = -i\lambda_p(t_{13}t_{32}^* + t_{12}t_{33}^*)$, $H_{22} = \epsilon_{xy} - \epsilon_p(|t_{21}|^2 + |t_{24}|^2)$, $H_{23} = -i\lambda_p(t_{21}t_{32}^* - t_{24}t_{33}^*)$, $H_{25} = h_{25}$, $H_{26} = h_{26} - \epsilon_p(t_{24}t_{32}^* + t_{21}t_{33}^*)$, $H_{33} = \epsilon_{z^2} - \epsilon_p(|t_{32}|^2 + |t_{33}|^2)$, and $H_{36} = h_{36}$. As shown in Figs. 8(g)–8(i), this model not only accurately reflects the low-energy dispersions but also captures the nontrivial topological properties of the system.

Because the building blocks of the Fe_2BrMgP monolayer are half Chern insulator FeBr, the above-mentioned spin-chirality-spatial locking phenomenon in edge states is expected. To show this phenomenon, we calculated the spatial and spin projections of edge states on one side of the Fe_2BrMgP nanoribbon. As shown in Fig. 7(a), the edge states are fully spin polarized, and the edge states with different spins have different chirality, indicating that the spin and chirality of edge states are locked. Furthermore, the edge states with different spins or chiralities are distributed in different areas of the border, shown in Fig. 7(b).

The robustness of the gapless edge states was tested by applying a uniform FM exchange field along the x direction [Fig. 7(d)] and a doped local magnetic impurity [Fig. 7(e)] at the edge region of the Fe_2BrMgP monolayer. To simulate the effect of magnetic impurities, a local magnetic exchange field perpendicular to the AFM order of the system was added to the spin space at an Fe site in the surface Hamiltonian in the iterative solution of the surface Green's function for the semi-infinite system. When the strength of exchange field or magnetic impurities was not very large, the edge states always remained gapless, which demonstrates that the nontrivial edge states of the Fe_2BrMgP monolayer are robust to spin-mixing FM exchange fields and disorder magnetic impurities.

We have some remarks before closing. First, the high C_s (greater than 1) becomes meaningful, and the high even C_s is distinct from the $C_s = 0$ in our proposal. Second, the number of C_s and spin transport channels can be expanded by increasing the number of stacked layers. Due to $\mathcal{PT}$ symmetry and the half property of the constituent units, scattering in the transport channels of our AFM-QSH insulators is negligible. Third, although the z-direction electronic field can open gaps in edge states, it cannot completely destroy the edge states due to the topological response [Fig. 7(f)]. The gap in edge states and hence spin Hall conductance in our systems can be effectively tuned by a z-direction electronic field, which is beneficial for further applications. Moreover, due to spin-chirality-spatial locking of edge states, the z-direction electronic field will break the balance of carrier concentration between transport channels with different chiralities in the upper and lower spaces, and thus there is a net charge flow generated. This feature does not exist in traditional $\mathbb{Z}_2$ QSH insulator.

In summary, we propose a general proposal to realize AFM QSH insulators by stacking half-QAH insulators in a way that preserves the $\mathcal{PT}$ symmetry. The obtained AFM QSH insulators can have multiple pairs of dissipationless spin transport channels, depending on the number of stacking layers, which are characterized by a high C_s. Using two concrete materials examples, Fe_2BrMgP monolayer and TiTe bilayer, we show that both intercalation and vdW stacks can be used to realize the proposed AFM QSH insulators. The gapless edge states and topological invariants (high C_s) of these materials have been proven to be robust through several tests, demonstrating their resilience to diluted magnetic impurities and weak magnetic fields. Furthermore, spin-chirality-spatial locking of edge states in the proposed AFM QSH insulators is revealed. The edge states and spin Hall conductances in these systems can be effectively tuned by a z-direction electronic field. These results are beneficial for realizing low-power and high-efficiency topological spintronics devices with easy manipulation.

ACKNOWLEDGMENTS

We thank Prof. Supeng Kou for a very helpful discussion. This work was supported by National Natural Science Foundation of China under Grants No. 11904101, No. 11604134, No. 11874117, No. 11904250, and No. 12174059 and the Natural Science Foundation of Shanghai under Grant No. 21ZR1408200.

APPENDIX A: PROOF FOR DOUBLE DEGENERACY IN $\mathcal{PT}$ INVARIANT SYSTEMS

$\mathcal{PT}$ symmetry is an antiunitary symmetry with the product $(\mathcal{PT})^2 = -1$. Arbitrary k is invariant under $\mathcal{PT}$, since $\mathcal{P}$ and $\mathcal{T}$ both map k to $-k$. The Hamiltonian $H(k)$ for a $\mathcal{PT}$

invariant system should satisfy

$$[H(k), \mathcal{PT}] = 0. \tag{A1}$$

For an arbitrary eigenstate $|\psi(k)\rangle$ of $H(k)$ with energy $E(k)$, its $\mathcal{PT}$ pair $|\phi(k)\rangle = \mathcal{PT}|\psi(k)\rangle$ is also an eigenstate with k and $E(k)$:

$$\begin{aligned} H(k)|\phi(k)\rangle &= H(k)(\mathcal{PT}|\psi(k)\rangle) = \mathcal{PT}(H(k)|\psi(k)\rangle) \\ &= E(k)(\mathcal{PT}|\psi(k)\rangle) = E(k)|\phi(k)\rangle. \end{aligned} \tag{A2}$$

Furthermore, the $\mathcal{PT}$ symmetry yields that $|\psi(k)\rangle$ and $|\phi(k)\rangle$ are orthogonal to each other, $\langle\psi(k)|\phi(k)\rangle = 0$, because

$$\begin{aligned} \langle\psi(k)|\phi(k)\rangle &= \langle\mathcal{PT}\phi(k)|\mathcal{PT}\psi(k)\rangle \\ &= \langle\psi(k)|(\mathcal{PT})^2|\phi(k)\rangle = -\langle\psi(k)|\phi(k)\rangle. \end{aligned} \tag{A3}$$

Therefore, every band in a $\mathcal{PT}$ invariant system must be doubly degenerate.

It is noted that although k is invariant under $\mathcal{PT}$, the eigenstate $|\psi(k)\rangle$ of a $\mathcal{PT}$ invariant Hamiltonian is not the eigenstate of $\mathcal{PT}$ due to its antiunitary property ($\mathcal{PT}$ transforms the $|\psi(k)\rangle$ into its complex conjugate). Under the basis of a $\mathcal{PT}$ doublet $\{\psi(k), (\mathcal{PT})\psi(k)\}$, we have

$$\begin{aligned} (\mathcal{PT})(\psi(k)) &= (\mathcal{PT})\psi(k), \\ (\mathcal{PT})[(\mathcal{PT})\psi(k)] &= (\mathcal{PT})^2\psi(k) = -\psi(k). \end{aligned} \tag{A4}$$

Thus, the $\mathcal{PT}$ operator takes the form of $-i\sigma_y = \left(\begin{smallmatrix} 0 & -1 \\ 1 & 0 \end{smallmatrix}\right)$ under this basis.

APPENDIX B: PROOF FOR GAP OPENING OF DIRAC POINTS AT THE $\widetilde{C}_{2x}$ ($\widetilde{C}_{2y}$) INVARIANT k LINES

The transformation of space coordinates, spin moments s, and momentum k under $\mathcal{PT}$ and $\widetilde{C}_{2x}$ are listed below:

$$(x, y, z) \xrightarrow{\mathcal{PT}} (-x, -y, -z), \tag{B1}$$

$$(s_x, s_y, s_z) \xrightarrow{\mathcal{PT}} (-s_x, -s_y, -s_z), \tag{B2}$$

$$(k_x, k_y, k_z) \xrightarrow{\mathcal{PT}} (k_x, k_y, k_z), \tag{B3}$$

$$(x, y, z) \xrightarrow{\widetilde{C}_{2x}} (x + a/2, -y, -z), \tag{B4}$$

$$(s_x, s_y, s_z) \xrightarrow{\widetilde{C}_{2x}} (s_x, -s_y, -s_z), \tag{B5}$$

$$(k_x, k_y, k_z) \xrightarrow{\widetilde{C}_{2x}} (k_x, -k_y, -k_z). \tag{B6}$$

From the transformation of spin moments s under $\mathcal{PT}$, we can obtain the relation between spin operator $\hat{s}_z$ and $\mathcal{PT}$,

$$(\mathcal{PT})^{-1}\hat{s}_z\mathcal{PT} = -\hat{s}_z, \tag{B7}$$

which means that $\hat{s}_z$ and $\mathcal{PT}$ are anticommutative: $\{\hat{s}_z, \mathcal{PT}\} = 0$.

The transformation of the square of $\widetilde{C}_{2x}$ is given as

$$(x, y, z) \xrightarrow{\widetilde{C}_{2x}} (x + a/2, -y, -z) \xrightarrow{\widetilde{C}_{2x}} (x + a, y, z), \tag{B8}$$

thus, the square of $\widetilde{C}_{2x}$ yields a unit vector translation along the x direction,

$$\widetilde{C}_{2x}^2 = -T(100) = -e^{ik_x}, \tag{B9}$$

where the minus sign of $-T(100)$ originates from the 2π rotation of spin. So, the eigenvalues of $\widetilde{C}_{2x}$ are $g_\pm = \pm ie^{ik_x/2}$.

By successively applying the symmetry operators $\widetilde{C}_{2x}$ and $\mathcal{PT}$, we have

$$(x, y, z) \xrightarrow{\widetilde{C}_{2x}} (x + a/2, -y, -z) \xrightarrow{\mathcal{PT}} (-x - a/2, y, z), \tag{B10}$$

$$(s_x, s_y, s_z) \xrightarrow{\widetilde{C}_{2x}} (s_x, -s_y, -s_z) \xrightarrow{\mathcal{PT}} (-s_x, s_y, s_z), \tag{B11}$$

$$(x, y, z) \xrightarrow{\mathcal{PT}} (-x, -y, -z) \xrightarrow{\widetilde{C}_{2x}} (-x + a/2, y, z), \tag{B12}$$

$$(s_x, s_y, s_z) \xrightarrow{\mathcal{PT}} (-s_x, -s_y, -s_z) \xrightarrow{\widetilde{C}_{2x}} (-s_x, s_y, s_z). \tag{B13}$$

Therefore, the communication relation between $\widetilde{C}_{2x}$ and $\mathcal{PT}$ satisfies

$$\widetilde{C}_{2x}(\mathcal{PT}) = e^{ik_x}(\mathcal{PT})\widetilde{C}_{2x}. \tag{B14}$$

The eigenstate $|\psi(k)\rangle$ labeled with a $\widetilde{C}_{2x}$ invariant k can carry the eigenvalues $g_\pm = \pm ie^{ik_x/2}$ of $\widetilde{C}_{2x}$. Without loss of generality, let the eigenvalue of $|\psi(k)\rangle$ be $g_+ = +ie^{ik_x/2}$. Then one can show the $\mathcal{PT}$ partner $|\phi(k)\rangle = (\mathcal{PT})|\psi(k)\rangle$ is the eigenstate of $\widetilde{C}_{2x}$ with $g_- = -ie^{ik_x/2}$ eigenvalue as well:

$$\begin{aligned} \widetilde{C}_{2x}[(\mathcal{PT})|\psi(k)\rangle] &= e^{ik_x}(\mathcal{PT})[\widetilde{C}_{2x}|\psi(k)\rangle] \\ &= e^{ik_x}(\mathcal{PT})[ie^{ik_x/2}|\psi(k)\rangle] \\ &= e^{ik_x}(-ie^{-ik_x/2})[(\mathcal{PT})|\psi(k)\rangle] \\ &= g_-[(\mathcal{PT})|\psi(k)\rangle]. \end{aligned} \tag{B15}$$

Clearly, in the $\widetilde{C}_{2x}$ invariant k path, $|\phi(k)\rangle$ and $|\psi(k)\rangle$ carry different representations. As a result, any band crossing (a fourfold Dirac point) on the $\widetilde{C}_{2x}$ invariant k path is generally unstable and can be gapped by SOC. The argument above applies to C_{2x}, C_{2y}, and $\widetilde{C}_{2y}$ as well.

For a $\mathcal{PT}$-symmetric system with the symmetries of n-fold rotation (C_n), the eigenstate $|\psi(k)\rangle$ of the system labeled with a C_n invariant k can carry the eigenvalues $(-1)^{1/n}e^{i2\pi/n} = e^{i3\pi/n}$ of C_n. Since C_n communicates with $\mathcal{PT}$ $[C_n, \mathcal{PT}] = 0$, the $\mathcal{PT}$ partner of the $|\psi(k)\rangle$ is also the eigenstate of C_n:

$$\begin{aligned} C_n[(\mathcal{PT})|\psi(k)\rangle] &= (\mathcal{PT})[C_n|\psi(k)\rangle] \\ &= (\mathcal{PT})[e^{i3\pi/n}|\psi(k)\rangle] \\ &= e^{-i3\pi/n}[(\mathcal{PT})|\psi(k)\rangle]. \end{aligned} \tag{B16}$$

The phase difference between the eigenvalues of $|\psi(k)\rangle$ and its $\mathcal{PT}$ partner is $\Delta = 2\pi(3/n)$. So long as $3/n \notin Z$, then the $|\psi(k)\rangle$ and its $\mathcal{PT}$ partner have different eigenvalues and thus belong to different irreducible representations. As a result, the

Dirac points located at the C_n invariant k points are usually not stable and can be gapped by SOC for $n = 2, 4, 6$.

APPENDIX C: THE CALCULATION FOR NEEL TEMPERATURE

To evaluate the Neel temperature of the Fe_2BrMgP monolayer, a Heisenberg model is built as:

$$H_0 = -J_1 \sum_{<i,j>} \boldsymbol{S_i} \cdot \boldsymbol{S_j} - J_2 \sum_{<<i,j\gg} \boldsymbol{S_i} \cdot \boldsymbol{S_j} - J_c \sum_{<<<i,j\gg>} \boldsymbol{S_i} \cdot \boldsymbol{S_j} - D \sum_i |S_i^e|^2, \tag{C1}$$

where $\boldsymbol{S_i}$ is the spin vector, $\boldsymbol{S_i^e}$ is the spin component along the easy axis, D is the strength for anisotropy, J_c and J_i $(i = 1, 2)$ denote the strengths for the exchange interactions parallel and perpendicular to the z direction, respectively. The values of J_i $(i = 1, 2)$, J_c and D can be extracted from the first-principles calculations with the equations

$$E_{\mathrm{FM}} = E_0 - 32J_1|S^2| - 32J_2|S^2| - 8J_c|S^2|, \tag{C2}$$

$$E_{\mathrm{AFM1}} = E_0 - 32J_1|S^2| - 32J_2|S^2| + 8J_c|S^2|, \tag{C3}$$

$$E_{\mathrm{AFM2}} = E_0 + 32J_2|S^2| + 8J_c|S^2|, \tag{C4}$$

$$E_{\mathrm{AFM3}} = E_0 + 32J_1|S^2| - 32J_2|S^2| + 8J_c|S^2|. \tag{C5}$$

The corresponding magnetic configurations in the above equations are shown in Fig. 3. The obtained values of parameters and the energy for different magnetic configurations are listed in Table II.

TABLE II. The relative total energy (meV per unit cell) for the Fe_2BrMgP monolayer with different magnetic state shown in Fig. 3, and the calculated magnetic coupling parameters of J_1, J_2, and J_c (meV), anisotropy parameter D (meV per Fe atom) and Neel temperature T_N (K).

FM	AFM-1	AFM-2	AFM-3	J_1	J_2	J_c	D	T_N
57.16	0	683.54	807.97	25.25	8.74	−7.15	2.69	125

[1] C. L. Kane and E. J. Mele, Z_2 Topological Order and the Quantumspin Hall Effect, Phys. Rev. Lett. **95**, 146802 (2005).

[2] C. L. Kane and E. J. Mele, Quantum Spin Hall Effect in Graphene, Phys. Rev. Lett. **95**, 226801 (2005).

[3] M. M. H. Polash, S. Yalameha, H. Zhou, K. Ahadi, Z. Nourbakhsh, and D. Vashaee, Topological quantum matter to topological phase conversion: Fundamentals, materials, physical systems for phase conversions, and device applications, Mater. Sci. Eng., R **145**, 100620 (2021).

[4] P. Tang, Q. Zhou, G. Xu, and S.-C. Zhang, Dirac fermions in an antiferromagnetic semimetal, Nat. Phys. **12**, 1100 (2016).

[5] D. N. Sheng, Z. Y. Weng, L. Sheng, and F. D. M. Haldane, Quantum Spin-Hall Effect and Topologically Invariant Chern Numbers, Phys. Rev. Lett. **97**, 036808 (2006).

[6] H. Li, L. Sheng, D. N. Sheng, and D. Y. Xing, Chern number of thin films of the topological insulator Bi_2Se_3, Phys. Rev. B **82**, 165104 (2010).

[7] D. Vanderbilt, *Berry Phases in Electronic Structure Theory: Electric Polarization, Orbital Magnetization and Topological Insulators*, 1st ed. (Cambridge University Press, Cambridge, England, 2018).

[8] M. Ezawa, High spin-Chern insulators with magnetic order, Sci. Rep. **3**, 3435 (2013).

[9] Y. Bai, L. Cai, N. Mao, R. Li, Y. Dai, B. Huang, and C. Niu, Doubled quantum spin Hall effect with high-spin Chern number in α-antimonene and α-bismuthene, Phys. Rev. B **105**, 195142 (2022).

[10] R. S. K. Mong, A. M. Essin, and J. E. Moore, Antiferromagnetic topological insulators, Phys. Rev. B **81**, 245209 (2010).

[11] C. Fang, M. J. Gilbert, and B. A. Bernevig, Topological insulators with commensurate antiferromagnetism, Phys. Rev. B **88**, 085406 (2013).

[12] C.-X. Liu, R.-X. Zhang, and B. K. VanLeeuwen, Topological nonsymmorphic crystalline insulators, Phys. Rev. B **90**, 085304 (2014).

[13] D. Zhang, M. Shi, T. Zhu, D. Xing, H. Zhang, and J. Wang, Topological Axion States in the Magnetic Insulator $MnBi_2Te_4$ with the Quantized Magnetoelectric Effect, Phys. Rev. Lett. **122**, 206401 (2019).

[14] J. Li, Y. Li, S. Du, Z. Wang, B.-L. Gu, S.-C. Zhang, K. He, W. Duan, and Y. Xu, Intrinsic magnetic topological insulators in van der Waals layered $MnBi_2Te_4$-family materials, Sci. Adv. **5**, eaaw5685 (2019).

[15] M. M. Otrokov, I. P. Rusinov, M. Blanco-Rey, M. Hoffmann, A. Y. Vyazovskaya, S. V. Eremeev, A. Ernst, P. M. Echenique, A. Arnau, and E. V. Chulkov, Unique Thickness-Dependent Properties of the van der Waals Interlayer Antiferromagnet $MnBi_2Te_4$ films, Phys. Rev. Lett. **122**, 107202 (2019).

[16] M. M. Otrokov, I. I. Klimovskikh, H. Bentmann, D. Estyunin, A. Zeugner, Z. S. Aliev, S. Gaß, A. U. B. Wolter, A. V. Koroleva, A. M. Shikin, M. Blanco-Rey, M. Hoffmann, I. P. Rusinov, A. Y. Vyazovskaya, S. V. Eremeev, Y. M. Koroteev, V. M. Kuznetsov, F. Freyse, J. Sánchez-Barriga, I. R. Amiraslanov *et al.*, Prediction and observation of an antiferromagnetic topological insulator, Nature (London) **576**, 416 (2019).

[17] X. Hu, N. Mao, H. Wang, Y. Dai, B. Huang, and C. Niu, Quantum spin Hall effect in antiferromagnetic topological heterobilayers, Phys. Rev. B **103**, 085109 (2021).

[18] C. Niu, H. Wang, N. Mao, B. Huang, Y. Mokrousov, and Y. Dai, Antiferromagnetic Topological Insulator with Nonsymmorphic Protection in Two Dimensions, Phys. Rev. Lett. **124**, 066401 (2020).

[19] Y. Yang, Z. Xu, L. Sheng, B. Wang, D. Y. Xing, and D. N. Sheng, Time-Reversal-Symmetry-Broken Quantum Spin Hall Effect, Phys. Rev. Lett. **107**, 066602 (2011).

[20] Y. Xue, B. Zhao, Y. Zhu, T. Zhou, J. Zhang, N. Li, H. Jiang, and Z. Yang, Novel Chern insulators with half-metallic edge states, NPG Asia Mater. **10**, e467 (2018).

[21] L. Liu, H. Huan, Y. Xue, H. Bao, and Z. Yang, Anisotropy-induced phase transitions in an intrinsic half-Chern insulator Ni_2I_2, Nanoscale **14**, 13378 (2022).

[22] W. Xu, J. Yi, H. Huan, B. Zhao, Y. Xue, and Z. Yang, Two-dimensional half Chern-Weyl semimetal with multiple screw axes, Phys. Rev. B **106**, 205108 (2022).

[23] Q. Sun, Y. Ma, and N. Kioussis, Two-dimensional Dirac spin-gapless semiconductors with tunable perpendicular magnetic anisotropy and a robust quantum anomalous Hall effect, Mater. Horiz. **7**, 2071 (2020).

[24] J. P. Perdew, K. Burke, and M. Ernzerhof, Generalized Gradient Approximation Made Simple, Phys. Rev. Lett. **77**, 3865 (1996).

[25] G. Kresse and J. Furthmüller, Efficient iterative schemes for *ab initio* total-energy calculations using a plane-wave basis set, Phys. Rev. B **54**, 11169 (1996).

[26] A. I. Liechtenstein, V. I. Anisimov, and J. Zaanen, Density-functional theory and strong interactions: Orbital ordering in Mott-Hubbard insulators, Phys. Rev. B **52**, R5467 (1995).

[27] A. A. Mostofi, J. R. Yates, Y.-S. Lee, I. Souza, D. Vanderbilt, and N. Marzari, Wannier90: A tool for obtaining maximally-localised Wannier functions, Comput. Phys. Commun. **178**, 685 (2008).

[28] Q. Wu, S. Zhang, H.-F. Song, M. Troyer, and A. A. Soluyanov, WannierTools: An open-source software package for novel topological materials, Comput. Phys. Commun. **224**, 405 (2018).

[29] J. Heyd, G. E. Scuseria, and M. Ernzerhof, Hybrid functionals based on a screened Coulomb potential, J. Chem. Phys. **118**, 8207 (2003).

[30] A. Togo, F. Oba, and I. Tanaka, First-principles calculations of the ferroelastic transition between rutile-type and $CaCl_2$-type SiO_2 at high pressures, Phys. Rev. B **78**, 134106 (2008).

[31] A. Togo and I. Tanaka, First principles phonon calculations in materials science, Scr. Mater. **108**, 1 (2015).

[32] S. Ullah, A. Ahmad, K. Alam, M. Usman, S. Khan, A. M. Alanazi, and F. Khan, Optical properties of topological semimetal Mx compounds (M = Ti, Zr, Hf and X = S, Se, Te) by first-principles calculation, available at SSRN 4291615 (2022), doi:10.2139/ssrn.4291615.

[33] P. W. Anderson, New approach to the theory of superexchange interactions, Phys. Rev. **115**, 2 (1959).

[34] J. B. Goodenough, Theory of the role of covalence in the perovskite-type manganites [La, M(II)]MnO_3, Phys. Rev. **100**, 564 (1955).

[35] J. Kanamori, Crystal distortion in magnetic compounds, J. Appl. Phys. **31**, S14 (1960).

[36] L. Matthes, S. Küfner, J. Furthmüller, and F. Bechstedt, Intrinsic spin Hall conductivity in one-, two-, and three-dimensional trivial and topological systems, Phys. Rev. B **94**, 085410 (2016).

[37] J. Qiao, J. Zhou, Z. Yuan, and W. Zhao, Calculation of intrinsic spin Hall conductivity by Wannier interpolation, Phys. Rev. B **98**, 214402 (2018).